INORGANIC CHEMISTRY FRONTIERS

RESEARCH ARTICLE

View Article Online
View Journal | View Issue

Cite this: *Inorg. Chem. Front.*, 2024, **11**, 3309

An unprecedented $\{Y_2 \subset Y_{10}\}$ type disk-like Y_{12} nanocluster featuring electroluminescence property in OLED device†

Lin-Ping Shi,[a] Wen-Liang Li,[a] Pu-Yue Wang,[a] Xiao-Ming Wu,*[b] Zhao-Quan Yao,*[a] Jiong-Peng Zhao *[a] and Fu-Chen Liu *[a]

Received 11th March 2024,
Accepted 18th April 2024

DOI: 10.1039/d4qi00635f

rsc.li/frontiers-inorganic

Although great efforts have been made to explore the exquisite rare-earth (RE) clusters, the design and construction of planar RE clusters with disk-like geometrical features are still scarce. Herein, a novel disk-like RE-cluster Y_{12} (abbreviated as **1**), formulated as $[Y_{12}(L)_{10}(CO_3)_4(NO_3)_2(\mu_3\text{-}OH)_6]$ (H_2L = 7,7′-(2-methyl-methylene)bis(8-quinolonol)) was synthesized successfully under solvothermal conditions. Owing to the template effect and fruitful coordination modes of NO_3^-, a novel $Y_2 \subset Y_{10}$ type structure with dual-core in the center position of the cluster, which distinguishes it from the traditional brucite-type disk-like RE-cluster was achieved. Based on the ESI-MS analysis, the possible assembly mechanism of $Y_5 \rightarrow Y_8 \rightarrow Y_{12}$ is proposed. The luminescence investigation illustrates that this cluster not only shows green emission in solid-state and common organic solvents but also has obvious electroluminescent performance, which can be used as the emitting layer in organic light-emitting diodes (OLEDs).

In the past few decades, great efforts have been devoted to the construction and investigation of the properties of polynuclear rare-earth (RE) clusters owing to not only their intriguing geometrical features and fascinating physical and chemical properties but also their potential applications in the field of single-molecule magnetism (SMM), magnetocaloric materials, catalysis, luminescence devices, *etc.*[1–5] Although some exclusive polynuclear RE-clusters, especially the lanthanide (Ln) cluster with different nuclear numbers and geometrical features, such as Ln_5, Ln_{10}, Ln_{12}, Ln_{18}, Ln_{20}, Ln_{22}, Ln_{24}, Ln_{27}, Ln_{28}, Ln_{36}, Ln_{37}, Ln_{38}, Ln_{48}, Ln_{60}, Ln_{76}, Ln_{104}, and Ln_{140}, have been reported,[6–21] the rational design and fabrication of exclusive polynuclear RE-clusters with high nuclear number ($n > 10$) and specific geometric conformation still remains a formidable challenge owing to the high coordination numbers, versatile coordination geometries of RE^{3+} ions, and mutual repulsion effect between the RE^{3+} ions with high positive charges.[12,13,22] Furthermore, the assembly process of the polynuclear rare earth clusters is mainly determined by RE^{3+} ion hydrolysis, which could produce the hydroxy intermediates for further assembly.[19] Thus, the construction conditions are always sensitive to the ratio of ligands/RE^{3+} ions and other external factors (*i.e.* temperature, pH, anions template, *etc.*). This will undoubtedly bring more obstacles to the design and synthesis of polynuclear RE-clusters directly.[23]

Up to now, most of the reported polynuclear RE-clusters exhibit stereo geometrical features such as cage-shaped,[12,13] ball-shaped,[6,14] windmill-shaped,[9] barrel-shaped,[16] drum-shaped,[17] and tubular-shaped,[19] which can be attributed to the diverse coordination modes and the poor directionality of the high-valent RE^{3+} ions. While, regulating the growth of RE^{3+} ions in a certain plane to form the exquisite disk-like cluster with a planar geometrical feature is hard to achieve. Heretofore, only a few cases of RE-clusters with planar structures have been reported.[24–27] The coordination modes in these disk-like RE-clusters are all similar to brucite in which the RE^{3+} ions are arranged in the hexagonal close-packing mode.[25–27] During the growth process, each RE^{3+} nuclear combines with six adjacent RE^{3+} ions *via* $\mu_3\text{-}OH^-/O^{2-}$ bridging, thus, the nuclear number of this type of RE-cluster needs to satisfy the relation "$1 + \Sigma_n 6n$" (n stands for the ring number in the Brucite structure), which will hinder the discovery of the novel planar RE-cluster with the other nuclear numbers.

[a]*TKL of Organic Solar Cells and Photochemical Conversion, School of Chemistry and Chemical Engineering, Tianjin University of Technology, Tianjin 300384, China. E-mail: yaozq@email.tjut.edu.cn, zhaojp@tjut.edu.cn, fcliu@tjut.edu.cn*
[b]*Key Laboratory of Display Materials and Photoelectric Devices, Ministry of Education, Tianjin Key Laboratory of Photoelectric Materials and Devices, National Demonstration Center for Experimental Function Materials Education, School of Materials Science and Engineering, Tianjin University of Technology, Tianjin 300384, China. E-mail: wxm@tjut.edu.cn*

†Electronic supplementary information (ESI) available: Additional crystallographic data. CCDC 2335670. For ESI and crystallographic data in CIF or other electronic format see DOI: https://doi.org/10.1039/d4qi00635f

Therefore, breaking the constraints of the brucite-type structure and discovering new coordination modes is highly desired in fabricating the new disk-like RE-clusters.

Besides, in order to control the growth of RE^{3+} ions toward the disk-like structure in a certain plane, the design and selection of the auxiliary ligands are also significant. Distinguishing with the commercial ligands, the *in situ* ligand formation strategy is one of the effective methods for rationally fabricating RE clusters in a certain direction.[13,27,28] Firstly, the *in situ* ligands formed by the oligomerization, decomposition, or rearrangement of raw ligands and solvents are always difficult or even impossible to synthesize by conventional organic synthesis methods could bring some specific coordination modes that could not only promote the RE^{3+} ions assembly in a specific direction but also induce polynuclear RE-clusters with intriguing architectures.[27] Secondly, the ligand formation process is relatively slow, which can remarkably avoid the formation of the precipitate caused by the fast reaction between metal ions and organic ligands, providing sufficient reaction time to form sophisticated coordination modes.[19] Last but not least, some anionic templates could be formed during *in situ* reactions, which has beneficial effects on the construction of polynuclear RE-clusters.[13] In addition, the mixed anions template strategy also proves great effect on the assembly of the polynuclear RE-cluster owing to not only their template effect to induce the formation of the clusters with specific geometrical features but also their negative charges, which can balance the positive charges of RE^{3+} ions to stabilize the cluster.[12,15]

Based on the combined strategy of the *in situ* reaction and the mixed anions template method, an unprecedented disk-like exquisite RE-cluster (**1**) with the formula of $[Y_{12}(L)_{10}(CO_3)_4(NO_3)_2(\mu_3\text{-}OH)_6]$ (H_2L = 7,7′-(2-methylmethylene) bis(8-quinolonol)) was designed and synthesized successfully. Structural analysis demonstrated that this disk-like Y_{12} can be split into the di-nuclear Y_2 subunit, which is located in the center of Y_{12} and the charming decanuclear ring-shaped Y_{10} subunit, which encapsulates the Y_2 core tightly. The whole Y_{12} cluster was surrounded by ten L^{2-} ligands, which were formed by the *in situ* reaction.[29,30] The linear geometrical feature and multi-coordination sites of these *in situ* ligands could regulate the cluster assembly in a specific direction. Moreover, instead of $\mu_3\text{-}OH^-/O^{2-}$ in the reported RE-clusters with the brucite structure, the triangular NO_3^- ions were introduced and anchored in this cluster to act as linkers and templates. Owing to the fruitful coordination sites and the negative charge, which could balance the superfluous positive charge, the rule of "$1 + \Sigma_n 6n$" in the brucite-type structure will be broken. Based on the combined effect between *in situ* ligands and anions template strategy, the unprecedented $Y_2 \subset Y_{10}$ disk cluster Ln-structure was achieved. The possible assembly mechanism was also confirmed by ESI-MS. Furthermore, owing to the obvious green luminescence and the good solubility of **1**, these exquisite RE-clusters were used as an emission layer to fabricate the OLED. The results provide a proof-of-concept and are of relevance to developing RE-clusters as emitting layers for OLEDs, providing a novel guideline for the application of RE-clusters.

The light-yellow quadrilateral single crystal of disk-like Y_{12}-cluster was obtained by the solvothermal reaction of $Y(NO_3)_3{\cdot}6H_2O$, 8-hydroxyquinoline and sodium carbonate in the mixed solution of EtOH and H_2O at 140 °C for 3d. Single crystal X-ray diffraction data indicates that this disk-like Y_{12}-cluster **1** crystallizes in the $P\bar{1}$ space group of the triclinic system (Table S1†). The length and width of the Y_{12}-cluster can reach 21.4 and 22.6 Å, respectively, which demonstrates that the structure of this cluster is approximately perfect disk-shape. As shown in Fig. 1, the whole Y_{12}-nanocluster consists of 12 Y^{3+} ions, ten *in situ* ligands (L^{2-}), six $\mu_3\text{-}OH^-$ groups, four CO_3^{2-} and two NO_3^-. In this structure, all the Y^{3+} ions exhibit octa-coordination modes and are tightly bridged by $\mu_3\text{-}OH^-$ or NO_3^-. Owing to the triangular coordination mode of $\mu_3\text{-}OH^-$ or NO_3^-, the twelve Y^{3+} ions are distributed in the equatorial plane to form the unprecedented disk-like Y/O core. The periphery of the Y/O core is surrounded by ten L^{2-} which is generated *via* the *in situ* reaction between 8-quinolonol and EtOH (Scheme S1†), and these ligands are located above and below the cluster plane, forming the unique double-layered five-leaf windmill structure to protect the stability of Y_{12}-cluster (Fig. 1a–c). Besides, four CO_3^{2-} ions are inserted in the center Y_2 subunit to balance the superfluous positive charges and stabilize the Y_{12} cluster.

In order to facilitate the analysis and investigation of the structural skeleton of **1**, this disk-like Y_{12}-cluster can be split into two types of cluster units: the center di-nuclear Y_2 subunit (type I) and the ring-shaped Y_{10} subunit (type II). In type I, the coordination environments of these two Y^{3+} ions are identical. Each Y^{3+} ion exhibits an octa-coordination mode defined by three O atoms from $\mu_3\text{-}OH^-$ ion, three O atoms from two CO_3^{2-} ions, and two O atoms from two NO_3^- ions and the coordination configuration is square antiprism (Fig. S1†). While in the type II subunit, the ten Y^{3+} ions in this ring-like structure have similar O_6N_2 octa-coordination modes. According to the different coordination environments, these Y^{3+} ions can be divided into three types, which are represented as Y1, Y2 and Y3. Atom Y1 is stabilized by two N atoms from two L^{2-} ligands, four O atoms from four independent L^{2-} ligands and two O atoms from one NO_3^- ion. Atom Y2 is attached to two N atoms from two L^{2-} ligands, four O atoms from four L^{2-} ligands, one O atom from NO_3^- ion and one O atom from $\mu_3\text{-}OH^-$ ion. While atom Y3 is connected by two N atoms from two L^{2-} ligands, four O atoms from four L^{2-} ligands and two O atoms from $\mu_3\text{-}OH^-$ ions (Fig. S1d†). According to the shape calculation, the coordination configuration of all these ten Y^{3+} ions are snub disphenoid (Fig. S1e†). Bridged by two $\mu_3\text{-}NO_3^-$ $\mu_3\text{-}NO_3^-$ and six $\mu_3\text{-}OH^-$, the Y_2 subunit is tightly anchored in the center position of the ring-like Y_{10} to form the unique $Y_2 \subset Y_{10}$ disk-like clusters, which are packaged by ten L^{2-} ligands in the same coordination pattern: $\mu_3\text{–}\eta^1\text{:}\eta^2\text{:}\eta^2\text{:}\eta^1$ (Fig. S1†). As shown in the crystal data of **1**, the bond length distances of Y–O are in the range from 2.274 to 2.444 Å, and those of Y–N are within 2.405–2.730 Å (Tables S2 and S3†), which are similar to

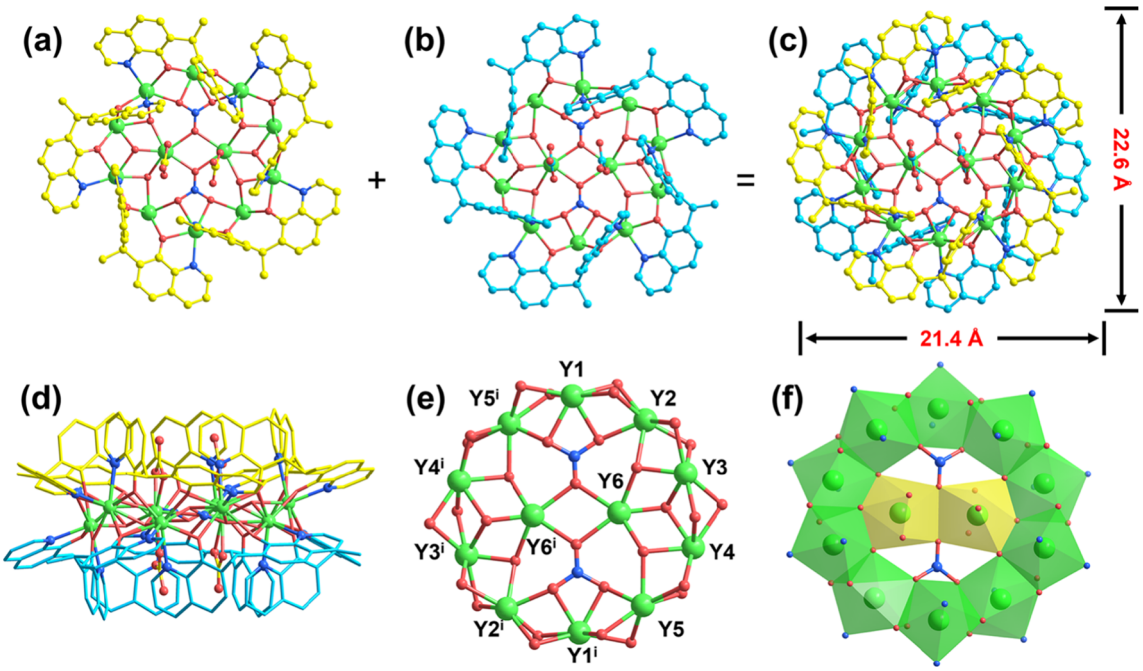

Fig. 1 (a) and (b) Parts of the Y_{12} cluster (**1**) above and below the cluster plane. (c) The top view of the whole molecular structure of **1**. (d) The side view of the Y_{12} cluster. (e) The diagram of the disk-like $Y_2 \subset Y_{10}$ cation core of **1**. (f) The coordinative environment of the two different types of Y^{3+} ions in **1**. Atom colors: Y green, C yellow and cyan, O red, N blue. All H atoms are omitted for clarity. Symmetry code: $^{i}1 - x, 1 - y, 1 - z$.

the reported Y cluster previously. Due to the structural similarity between CO_3^{2-} and NO_3^-, it is difficult to confirm the co-existence of these two anions in the Y_{12}-cluster using a single X-ray crystal diffraction technique, thus, FT-IR spectral measurements were performed. As shown in Fig. S2,† the main peaks of **1** are located at 3425 cm^{-1}, 1630 cm^{-1}, 1570 cm^{-1}, 1463 cm^{-1}, 1375 cm^{-1}, and 590 cm^{-1}. Among them, the peak at 3425 cm^{-1} corresponds to the stretching vibrations of the O–H bonds in μ_3-OH^- groups; those at 1630 cm^{-1} and 1570 cm^{-1} can be assigned to the stretching vibrations of C=N and C=C bonds in L^{2-} ligands; the peaks at 1463 cm^{-1} and 1375 cm^{-1} can be attributed to the stretching vibration of CO_3^{2-} and NO_3^- ions, respectively, which indicated the co-existence of the CO_3^{2-} and NO_3^- ions in the Y_{12}-cluster (Fig. S2b†). Interestingly, compared to the traditional μ_3-OH^- bridging ligands, NO_3^- ions have similar triangular geometrical features and more fruitful coordination modes. Using NO_3^- instead of the μ_3-OH^-/O^{2-} ions as the bridging ligands, the restriction of the "$1 + \Sigma_n 6n$" rule in traditional brucite-type RE-cluster is broken, with the formation of the Y_2 core, the outer shell is gradually assembled by Y_{10} to form the unprecedented core–shell $Y_2 \subset Y_{10}$ disk-like structure. After that, the adjacent Y_{12} clusters are connected *via* two different C–H···π interactions (C49–H49···π, d_1 = 2.767 Å; C34–H34···π, d_2 = 2.985 Å) (Table S4†) to generate the 2-dimensional supermolecule structure (Fig. 2) and further packed to form the extended 3D crystalline structure *via* the van der Waals' force. The 3D stacking diagram of the Y_{12} cluster (**1**) is shown in Fig. 2 and S1c.† To confirm the phase purity of the crystal sample of **1**, PXRD measurements were performed. As shown

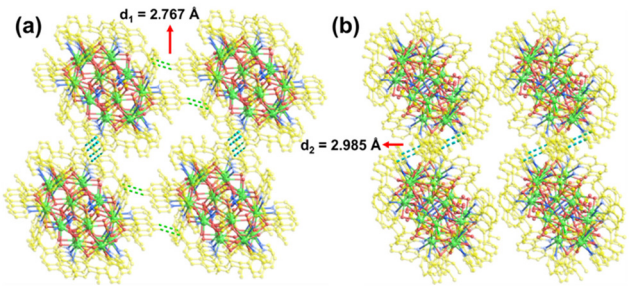

Fig. 2 (a) and (b) The views of the stacking modes of the Y_{12} cluster (**1**) along the *a* and *c*-axis.

in Fig. S2a,† the main characteristic diffraction peaks in the PXRD pattern of **1** can match well with the simulation, which indicates the high purity of the synthesized sample. The difference in the intensities between the experimental result and the simulation pattern can be attributed to the preferential selection of the crystal sample. The thermogravimetric analysis (TGA) suggested that before 370 °C, there was not any obvious weight loss in the Y_{12} cluster (Fig. S3†).

In order to further investigate the solution stability and the possible assembly mechanism of this unique disk-like Y_{12} cluster, the electrospray ionization mass spectrometry (ESI-MS) of Y_{12} cluster by dissolving the crystals in DMF and methanol and the crystal reaction solution in the range of m/z = 300–6000 have been collected, respectively (Fig. S4†). As shown in Table S1,† the formula weight of **1** is 4676.34, however, in ESI-MS spectra of **1** dissolved in DMF and MeOH, the mole-

cular ion peak of the Y_{12} cluster was not observed. The spectrum of **1** dissolved in DMF exhibits two prominent singly-charged ion peaks at m/z = 4469.601, and 4371.716 (Fig. S4†), which can be assigned to $[Y_{12}(L)_9(CO_3)_4(NO_3)_2(\mu_3\text{-}OH)_7(H_2O)_5]^+$ (cal. m/z 4469.080) and $[Y_{12}(L)_9(CO_3)_3(NO_3)_2(\mu_3\text{-}OH)_9(H_2O)]^+$ (cal. m/z 4371.025), respectively. Compared with the molecular formula of **1**, these two cations have the same Y_{12} cluster but contain more μ_3-OH^- and water and fewer L^{2-} ions, which indicates that the core Y_{12} cluster is stable in DMF and MeOH. Furthermore, the stability of the core Y_{12} cluster under the condition of ESI-MS measurement also paves the way for exploring the possible self-assembly mechanism. Comparing the ESI-MS spectrum of the Y_{12} cluster reaction solution to that in organic solvents, there are two obvious peaks that stand for two different fragment species with charge states of +3 and +2 can be observed at m/z = 709.169 and 1523.145, respectively. In detail, the peak at m/z = 709.169 can be assigned to $[Y_5(L)_3(HL)_2(NO_3)(\mu_3\text{-}OH)_3]^{3+}$ ions (cal. m/z = 709.83). While the peak, which is located at m/z = 1523.145 can be attributed to $[Y_8(L)_6(CO_3)_2(NO_3)_2(\mu_3\text{-}OH)_4(CH_3CH_2OH)_3]^{2+}$ ions (cal. m/z = 1523.765) (Table S5†). It is worth noting that compared to the high intensity of the peaks at m/z = 4469.601, and 4371.716 in the spectrum of Y_{12} dissolved in DMF, the similar peaks in the spectrum of the reaction solution can be negligible, instead, the intensities of the peaks at m/z = 709.169 and 1523.145 are much higher in the reaction solution, which means that during the self-assembly process, the Y^{3+} ions and the ligands were first constructed into Y_5 or Y_8 fragments, and then further assembled to form the Y_{12} clusters. Therefore, the possible assembly mechanism can be summarized as $Y_5 \rightarrow Y_8 \rightarrow Y_{12}$. As shown in Fig. S5,† firstly, the Y^{3+} ions occupy the periphery position and are bridged *via* the L^{2-} ligands, NO_3^- and μ_3-OH^- ions react to form the arc-shaped cluster (Y_5) which is similar to the crescent, then, the Y_5 cluster combine with other two Y^{3+} ions at the periphery position and one Y^{3+} ion, which is located in the core position, to produce the semi-circle-shaped Y_8 cluster. Finally, Y_8 connects the other four Y^{3+} ions *via* the bridging effect of NO_3^- and μ_3-OH^- ions to form the disk-like Y_{12} cluster. As far as we know, this is the first time to explore the possible assembly mechanism of the non-brucite type disk-like RE-cluster, which contains two RE^{3+} in the center position of the cluster.

One of the charming properties of the exquisite RE-clusters (especially Ln-cluster) is their unique photoluminescence emission derived from the f–f electronic transition, which has many distinctive optical attributes, *i.e.* large Stokes shifts, narrow line emission, and long lifetimes.[31,32] However, owing to the Laporte-forbidden of the 4f–4f transition, the Ln-clusters always need auxiliary organic ligands to act as "antenna" to achieve strong emission.[33] Distinguish with the normal exquisite Ln-cluster, in this work, the disk-like Y_{12} cluster (**1**) exhibits illustrious green light broad band emission, which can be attributed to the emission of the organic ligands (L^{2-}). In Fig. S6a,† the UV-vis absorption spectrum exhibits a wide range of absorption peaks in the range from 250 nm to 500 nm, which can be attributed to the π–π* electronic transition in organic ligands. According to the calculation results of the Kubelka–Munk function, the band gap of **1** is 2.25 eV indicating its semiconductor characteristic of **1** (Fig. S6b†). As shown in Fig. 3, the normalized excitation and emission spectra of **1** in different states have been measured at room temperature. In the excitation spectra of **1**, the peak profiles are quite different, and the maximum values are 440 nm (solid-state), 343 nm (in MeOH) and 424 nm (in DMF). While the emission spectra of this Y_{12} cluster (**1**) in the solid state and dissolved in MeOH or DMF exhibit a similar broad band single peak profile. Among them, the emission maximum value of **1** in the solid state is 533 nm, which is red-shifted by 50 nm relative to that of the pure L^{2-} ligands, this is very common for organic luminescence ligand-based coordination complexes, which can be attributed to the reduced nonplanar distance between the two quinoline groups in L^{2-}, due to the special coordination modes in this cluster.[34] As **1** is dissolved in MeOH or DMF, an obvious blueshift of the emission peak can be observed and the emission maximum value reached 510 nm (in MeOH) and 522 nm (in DMF), owing to the solvation effect. Besides, at room temperature, the photoluminescence quantum yield (Φ_F) of **1** is 4.95% with a nanosecond lifetime (Fig. S6c and d†). The short lifetime further demonstrates that the luminescence of **1** should be attributed to the ligand emission rather than the LMCT (ligand-to-metal charge transfer). On account of the good solubility and solvent stability in common organic solvents (DMF and MeOH) and the moderate luminescence emission property, this disk-like Y_{12} cluster can be the luminescent layer for assembling the light-emitting device.

In order to obtain a homogeneous film with a controlled distribution of the emission layers, the spin-coating method was used due to not only its economical properties but also this method has tiny influence on the photophysical properties of the luminescence materials.[35] In this work, DMF was chosen to disperse and dissolve the crystal sample of **1** to prepare the liquid precursor, then the complex film was pre-

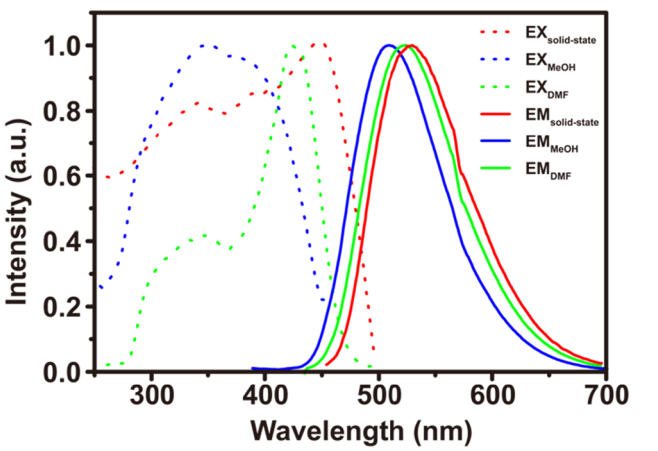

Fig. 3 Normalized excitation and emission spectra of **1** in the solid state and dissolved in methanol and DMF.

pared by the spin-coating method and the phase purity of this film was examined by PXRD (Fig. S7†). According to the SEM images of the thin film (Fig. S8a†), the nano-crystal particles of the Y_{12} clusters can be distributed on the ITO with uniform morphology. Furthermore, the EDX mapping images reflect the uniform distribution of Y, C, N, and O in this thin film sample (Fig. S8b–f†). The UV-vis absorption and photoluminescence spectra of film sample **1** are shown in Fig. S9.† Similar to the solid sample, the absorption spectrum of the film sample also exhibits a wide-range absorption peak in the range from 250 to 500 nm. Under the 350 nm excitation, the film sample displays an obvious green emission color and the emission spectrum of **1** in the film sample exhibits a broad band centered at 515 nm, which is very similar to those recorded in the solid state and dissolved in DMF. Based on the luminescence property, the film sample of **1** can be a good candidate as the luminescent layer in an OLED device. As shown in Fig. 4a and b, the entire OLED device was assembled by the indium-tin-oxide (ITO) coated glass substrate as the anode, the poly(3,4-ethylenedioxythiophene): polystyrene sulfonate (PEDOT:PSS, 40 nm) as the hole transport layer, Y_{12}-cluster film as a luminescent layer (110 nm), the 1,3,5-tris(1-phenyl-1*H*-benzimidazol-2-yl)benzene (TPBi, 40 nm) as the electron transport layer, the LiF layer (1 nm) as the electron injection layer. Finally, 120 nm aluminum film was evaporated on top of the device as the cathode. The electroluminescence (EL) spectrum indicates that this OLED device with 40 nm PEDOT:PSS and 40 nm TPBi could exhibit a wide range of emission peaks in the range from 450 to 650 nm, the maximum is located at 532 nm (Fig. 4c). The CIE chromaticity coordinates were calculated to be (0.332, 0.514), which are located in the green light area (Fig. 4e). The photograph of the emission color further demonstrates the green light emission of the OLED. According to the voltage–current density–luminance (*J*–*V*–*L*) curves (Fig. 4d), the turn-on voltage is as low as 4 V with a luminance of 3 cd m^{-2}. Besides, the luminance of this OLED shows a positive correlation depending on the voltage, and the maximum luminance of 84 cd m^{-2} can be obtained under 9 V before the degradation of the device. Although the performance of this Y_{12}-cluster-based OLED device is not comparable to the commercial devices or other reported metal–organic complexes (Table S6†),[36,37] this is the first systematic investigation on the EL performance of the larger RE-cluster (RE_n $n > 10$) as the emitter.

In summary, based on the combined effect of the *in situ* ligands, formation strategy and the anions template strategy, the rule of the "$1 + \Sigma_n 6n$" in the traditional brucite-type RE-cluster was broken. An unprecedented disk-like Y_{12} cluster with $Y_2 \subset Y_{10}$ type structure was synthesized. The structural analysis demonstrated that the two Y^{3+} ions form the Y_2 core, which was located in the center position, while the other ten Y^{3+} ions were bridged by the *in situ* ligands to form the ring-like subunit and encapsulate the Y_2 core tightly. The ESI-MS of **1** not only revealed that the metal skeleton of the Y_{12} cluster has good solubility and stability in some common organic solvents (DMF and MeOH) but also indicated the possible assembly mechanism could be $Y_5 \rightarrow Y_8 \rightarrow Y_{12}$. Furthermore, owing to the noticeable green light emission property, we successfully fabricated the green OLED based on the Y_{12} cluster as a luminescence layer, and the device presents obvious electroluminescent characteristics with a luminance of 84 cd m^{-2} at 9 V. This work not only proposes a novel strategy for design and synthesis the disk-like RE-clusters but also provides a proof-of-concept for the application of the exquisite RE-clusters in the field of OLEDs.

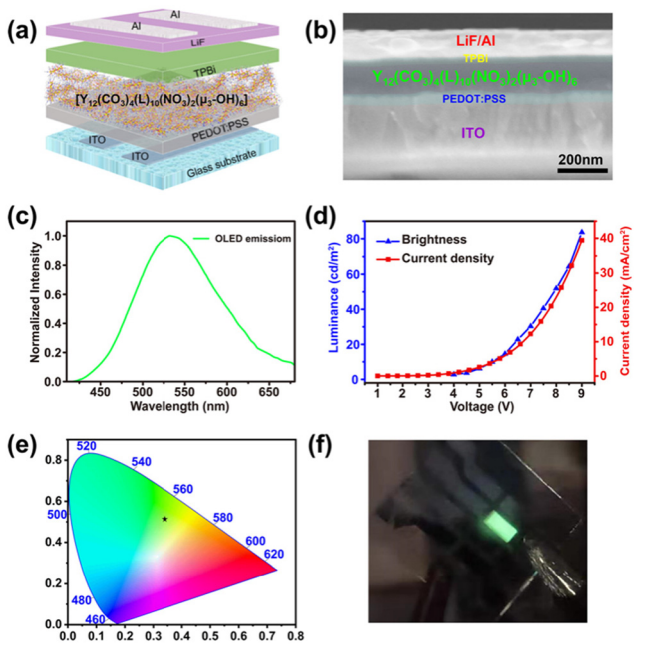

Fig. 4 (a) The diagram of the OLED device structure. (b) SEM cross-section images of the device. (c) The electroluminescence spectrum of the device. (d) Current density–voltage–luminance (*J*–*V*–*L*) curves of the device. (e) The CIE coordinate diagram of the device. (f) The photograph of the green OLED.

Author contributions

J.-P. Zhao and F.-C. Liu designed the project, L.-P. Shi, W.-L. Li, P.-Y. Wang synthesized the complexes. L.-P. Shi and X.-M. Wu conducted property testing. Z.-Q. Yao and J.-P. Zhao analysed the results. And L.-P. Shi, Z.-Q. Yao and J.-P. Zhao wrote the manuscript.

Conflicts of interest

There are no conflicts of interest to declare.

Acknowledgements

This work was supported by the NSFC of China (22271217, 21571139, 22035003 and 22001132).

References

1 X.-Y. Zheng, J. Xie, X.-J. Kong, L.-S. Long and L.-S. Zheng, Recent advances in the assembly of high-nuclearity lanthanide clusters, *Coord. Chem. Rev.*, 2019, **378**, 222–236.

2 X.-Y. Zheng, X.-J. Kong, Z. Zheng, L.-S. Long and L.-S. Zheng, High-nuclearity lanthanide-containing clusters as potential molecular magnetic coolers, *Acc. Chem. Res.*, 2018, **51**, 517–525.

3 X.-Z. Li, C.-B. Tian and Q.-F. Su, Coordination-directed self-assembly of functional polynuclear lanthanide supramolecular architectures, *Chem. Rev.*, 2022, **122**, 6374–6458.

4 Z.-H. Pan, Z.-Z. Weng, X.-J. Kong, L.-S. Long and L.-S. Zheng, Lanthanide-containing clusters for catalytic water splitting and CO_2 conversion, *Coord. Chem. Rev.*, 2022, **457**, 214419.

5 S. Shinoda and H. Tsukube, Luminescent lanthanide complexes as analytical tools in anion sensing, pH indication and protein recognition, *Analyst*, 2011, **136**, 431–435.

6 J.-B. Peng, X.-J. Kong, Y.-P. Ren, L.-S. Long, R.-B. Huang and L.-S. Zheng, Trigonal bipyramidal Dy_5 cluster exhibiting slow magnetic relaxation, *Inorg. Chem.*, 2012, **51**, 2186–2190.

7 S.-J. Liu, J.-P. Zhao, J. Tao, J.-M. Jia, S.-D. Han, Y. Li, Y.-C. Chen and X.-H. Bu, An unprecedented decanuclear GdIII cluster for magnetic refrigeration, *Inorg. Chem.*, 2013, **52**, 9163–9165.

8 J. Hao, L. Geng, J. Zheng, J. Wei, L. Zhang, R. Feng, J. Zhao, Q. Li, J. Pang and X.-H. Bu, Ligand induced double-chair conformation Ln_{12} nanoclusters showing multifunctional magnetic and proton conductive properties, *Inorg. Chem.*, 2022, **61**, 3690–3696.

9 Q. Wang, Y.-T. Yu, J.-N. Wang, J.-N. Li, X. Fan and Y. Xu, Two windmill-shaped Ln_{18} nanoclusters exhibiting high magnetocaloric effect and luminescence, *Inorg. Chem.*, 2023, **62**, 3162–3169.

10 W.-Q. Lin, X.-F. Liao, J.-H. Jia, J.-D. Leng, J.-L. Liu, F.-S. Guo and M.-L. Tong, Lanthanide oxide clusters: from tetrahedral $[Dy_4(\mu_4\text{-}O)]^{10+}$ to supertetrahedral $[Ln_{20}(\mu_4\text{-}O)_{11}]^{38+}$ (Ln = Tb, Dy, Ho, Er), *Chem. – Eur. J.*, 2013, **19**, 12254–12258.

11 Li.-X. Chang, G. Xiong, L. Wang, P. Cheng and B. Zhao, A 24-Gd nanocapsule with a large magnetocaloric effect, *Chem. Commun.*, 2013, **49**, 1055–1057.

12 X.-Y. Zheng, J.-B. Peng, X.-J. Kong, L.-S. Long and L.-S. Zheng, Mixed-anion templated cage-like lanthanide clusters: Gd_{27} and Dy_{27}, *Inorg. Chem. Front.*, 2016, **3**, 320–325.

13 Q. Wang, S.-H. Lu, L.-X. Xu, J.-L. Wang, Y.-T. Yu, X. Bai, H. Mei and Y. Xu, $C_2O_4^{2-}$-templated cage-shaped Ln_{28} (Ln = Gd, Eu) nanoclusters with magnetocaloric effect and luminescence, *Inorg. Chem. Front.*, 2023, **10**, 4109–4116.

14 M. Wu, F. Jiang, X. Kong, D. Yuan, L. Long, S. A. Al-Thabaiti and M. Hong, Two polymeric 36-metal pure lanthanide nanosize clusters, *Chem. Sci.*, 2013, **4**, 2104–3109.

15 Y. Zhou, X.-Y. Zheng, J. Cai, Z.-F. Hong, Z.-H. Yan, X.-J. Kong, Y.-P. Ren, L.-S. Long and L.-S. Zheng, Three Giant Lanthanide Clusters Ln_{37} (Ln = Gd, Tb, and Eu) Featuring A Double-Cage Structure, *Inorg. Chem.*, 2017, **56**, 2037–2041.

16 F.-S. Guo, Y.-C. Chen, L.-L. Mao, W.-Q. Li, J.-D. Leng, R. Tarasenko, M. Orendáč, J. Prokleška, V. Sechovský and M.-L. Tong, *Chem. – Eur. J.*, 2013, **19**, 14876–14885.

17 L. Chen, J.-Y. Guo, X. Xu, W.-W. Ju, D. Zhang, D.-R. Zhu and Y. Xu, A novel 2-D coordination polymer constructed from high-nuclearity waist drum-like pure Ho_{48} clusters, *Chem. Commun.*, 2013, **49**, 9728–9730.

18 X.-M. Luo, Z.-B. Hu, Q.-F. Lin, W. Cheng, J.-P. Cao, C.-H. Cui, H. Mei, Y. Song and Y. Xu, Exploring the performance improvement of magnetocaloric effect based Gd-exclusive cluster Gd_{60}, *J. Am. Chem. Soc.*, 2018, **140**, 11219–11222.

19 X.-Y. Li, H.-F. Su, Q.-W. Li, R. Feng, H.-Y. Bai, H.-Y. Chen, J. Xu and X.-H. Bu, A giant Dy_{76} cluster: a fused bi-nanopillar structural model for lanthanide clusters, *Angew. Chem., Int. Ed.*, 2019, **58**, 10184–10188.

20 J.-Bo. Peng, X.-J. Kong, Q.-C. Zhang, M. Orendáč, J. Prokleška, Y.-P. Ren, L.-S. Long, Z. Zheng and L.-S. Zheng, Beauty, symmetry, and magnetocaloric effect—four-shell keplerates with 104 lanthanide atoms, *J. Am. Chem. Soc.*, 2014, **136**, 17938–17941.

21 X.-Y. Zheng, Y.-H. Jiang, G.-L. Zhuang, D.-P. Liu, H.-G. Liao, X.-J. Kong, L.-S. Long and L.-S. Zheng, A gigantic molecular wheel of $\{Gd_{140}\}$: a new member of the molecular wheel family, *J. Am. Chem. Soc.*, 2017, **139**, 18178–18181.

22 D. Shi, X. Yang, Z. Xiao, X. Liu, H. Chen, Y. Ma, D. Schipper and R. A. Jones, A 42-metal Yb(III) nanowheel with NIR luminescent response to anions, *Nanoscale*, 2020, **12**, 1384–1388.

23 T.-Q. Song, J. Dong, A.-F. Yang, X.-J. Che, H.-L. Gao, J.-Z. Cui and B. Zhao, *Inorg. Chem.*, 2018, **57**, 3144–3150.

24 J.-N. Li, N.-F. Li, J.-L. Wang, X.-M. Liu, Q.-D. Ping, T.-T. Zang, H. Mei and Y. Xu, *Dalton Trans.*, 2021, **50**, 13925–13931.

25 J. W. Sharples, Y.-Z. Zheng, F. Tuna, E. J. L. McInnes and D. Collison, Lanthanide discs chill well and relax slowly, *Chem. Commun.*, 2011, **47**, 7650–7652.

26 Y.-L. Li, H.-L. Wang, Z.-H. Zhu, J. Li, H.-H. Zou, J.-M. Peng and F.-P. Liang, Truncation reaction regulates the out-to-in growth mechanism to decrypt the formation of brucite-like dysprosium clusters, *Dalton Trans.*, 2022, **51**, 197–202.

27 J.-M. Peng, H.-L. Wang, Z.-H. Zhu, J. Bai, F.-P. Liang and H.-H. Zou, Series of the largest dish-shaped dysprosium nanoclusters formed by in situ reactions, *Inorg. Chem.*, 2022, **61**, 6094–6100.

28 Y. Zhu, F. Luo, Y.-M. Song, X.-F. Feng, M.-B. Luo, Z.-W. Liao, G.-M. Sun, X.-Z. Tian and Z.-J. Yuan, *Cryst. Growth Des.*, 2012, **12**, 2158–2161.

29 M.-M. Wu, J.-Y. Wang, R. Sun, C. Zhao, J.-P. Zhao, G.-B. Che and F.-C. Liu, The design of dual-emissive composite material $[Zn_2(HL)_3]^+$@MOF–5 as self-calibrating

luminescent sensors of Al^{3+} ions and monoethanolamine, *Inorg. Chem.*, 2017, **56**, 9555–9562.

30 X.-W. Liang, L.-L. Zhang, T. Zhang, J.-P. Zhao and F.-C. Liu, Supramolecular isomorphic dodecanuclear cobalt clusters with the same metal shell but different core ligands, *Dalton Trans.*, 2022, **51**, 8491–8496.

31 M. Pan, W.-M. Liao, S.-Y. Yin, S.-S. Sun and C.-Y. Su, Single-phase white-light-emitting and photoluminescent color-tuning coordination assemblies, *Chem. Rev.*, 2018, **118**, 8889–8935.

32 D. A. Gálico, C. M. S. Calado and M. Murugesu, Lanthanide molecular cluster-aggregates as the next generation of optical materials, *Chem. Sci.*, 2023, **14**, 5827–5841.

33 F. Saraci, V. Quezada-Novoa, P. R. Donnarumma and A. J. Howarth, Rare-earth metal–organic frameworks: from structure to applications, *Chem. Soc. Rev.*, 2020, **49**, 7949–7977.

34 J.-J. Pang, Z.-Q. Yao, K. Zhang, Q.-W. Li, Z.-X. Fu, R. Zheng, W. Li, J. Xu and X.-H. Bu, Real-time in situ volatile organic compound sensing by a dual- emissive polynuclear Ln-MOF with pronounced LnIII luminescence response, *Angew. Chem., Int. Ed.*, 2023, **62**, e202217456.

35 C. Kaiyasuan, V. Somjit, B. Boekfa, D. Packwood, P. Chasing, T. Sudyoadsuk, K. Kongpatpanich and V. Promarak, intrinsic hole mobility in luminescent metal–organic frameworks and its application in organic light-emitting diodes, *Angew. Chem., Int. Ed.*, 2022, **61**, e202117608.

36 X. Feng, J.-G. Yang, J. Miao, C. Zhong, X. Yin, N. Li, C. Wu, Q. Zhang, Y. Chen, K. Li and C. Yang, Au···H-C interactions support a robust thermally activated delayed fluorescence (TADF) gold(I) complex for OLEDs with little efficiency roll-off and good stability, *Angew. Chem., Int. Ed.*, 2022, **61**, e202209451.

37 Y. Hu, J. Miao, T. Hua, Z. Huang, Y. Qi, Y. Zou, Y. Qiu, H. Xia, H. Liu, X. Cao and C. Yang, Efficient selenium-integrated TADF OLEDs with reduced roll-off, *Nat. Photonics*, 2022, **16**, 803–960.